Site-specifically labeled CA19.9-targeted immunoconjugates for the PET, NIRF, and multimodal PET/NIRF imaging of pancreatic cancer

Jacob L. Houghton[a,b], Brian M. Zeglis[a,c], Dalya Abdel-Atti[a,b], Robert Aggeler[d], Ritsuko Sawada[e], Brian J. Agnew[d], Wolfgang W. Scholz[e], and Jason S. Lewis[a,b,1]

[a]Department of Radiology, Memorial Sloan Kettering Cancer Center, New York, NY 10075; [b]Program in Molecular Pharmacology and Chemistry, Memorial Sloan Kettering Cancer Center, New York, NY 10075; [c]Department of Chemistry, Hunter College and the Graduate Center of the City University of New York, New York, NY 10065; [d]Foundational Biology Group, Thermo Fisher Scientific, Eugene, OR 97402; and [e]Mabvax, San Diego, CA 92121

Edited by Michael E. Phelps, University of California, Los Angeles, CA, and approved November 4, 2015 (received for review April 30, 2015)

Molecular imaging agents for preoperative positron emission tomography (PET) and near-infrared fluorescent (NIRF)-guided delineation of surgical margins could greatly enhance the diagnosis, staging, and resection of pancreatic cancer. PET and NIRF optical imaging offer complementary clinical applications, enabling the noninvasive whole-body imaging to localize disease and identification of tumor margins during surgery, respectively. We report the development of PET, NIRF, and dual-modal (PET/NIRF) imaging agents, using 5B1, a fully human monoclonal antibody that targets CA19.9, a well-established pancreatic cancer biomarker. Desferrioxamine (DFO) and/or a NIRF dye (FL) were conjugated to the heavy-chain glycans of 5B1, using a robust and reproducible site-specific (ss) labeling methodology to generate three constructs (^{ss}DFO-5B1, ^{ss}FL-5B1, and ^{ss}dual-5B1) in which the immunoreactivity was not affected by the conjugation of either label. Each construct was evaluated in a s.c. xenograft model, using CA19.9-positive (BxPC3) and -negative (MIAPaCa-2) human pancreatic cancer cell lines. Each construct showed exceptional uptake and contrast in antigen-positive tumors with negligible nonspecific uptake in antigen-negative tumors. Additionally, the dual-modal construct was evaluated in an orthotopic murine pancreatic cancer model, using the human pancreatic cancer cell line, Suit-2. The ^{ss}dual-5B1 demonstrated a remarkable capacity to delineate metastases and to map the sentinel lymph nodes via tandem PET-computed tomography (PET/CT) and NIRF imaging. Fluorescence microscopy, histopathology, and autoradiography were performed on representative sections of excised tumors to visualize the distribution of the constructs within the tumors. These imaging tools have tremendous potential for further preclinical research and for clinical translation.

pancreatic cancer | CA19.9 | molecular imaging | PET imaging

Pancreatic ductal adenocarcinoma (PDAC) is currently the fourth leading cause of cancer mortality and is expected to surpass both colorectal and breast cancer in total annual deaths by 2030 (1, 2). Surgical resection of the pancreas is the only curative treatment, but the presence of metastases precludes over 80% of patients from resection ab initio (3). The overall 5-y survival rate is ∼5%, and for those who qualify for surgical resection, the 5-y survival rate is only 25% due to the high incidence of undiscovered metastases (4, 5). Further complicating this dire situation, patients with PDAC are regularly misdiagnosed or understaged, confounding treatment strategies and preventing proper enrollment in clinical trials. Many of these problems could be avoided and outcomes improved if adequate clinical tools for diagnosing, staging, and treating PDAC were available.

Positron emission tomography (PET) is a promising technological platform for detecting, staging, and monitoring the progression or regression of many solid tumors, including PDAC. Optical imaging is a complementary platform that makes possible the accurate identification of tumor tissue in an intraoperative setting, which was recently demonstrated in human patients with ovarian cancer (6). Currently, the only Food and Drug Administration approved imaging agent for PDAC is 2-deoxy-2-[^{18}F]-fluoro-*D*-glucose (FDG). FDG PET imaging relies on increased tumor metabolism relative to nonmalignant cells (Warburg effect) (7). However, FDG has numerous shortcomings when it comes to PDAC, including unreliable detection of small primary lesions (<7 mm) (8) or liver metastases (<1 cm) (9), an inherent inability to discriminate between benign disease (i.e., pancreatitis) and malignancy (10), and decreased tumor avidity for FDG upon chemo- or radiation therapy (11). The development of an arsenal of imaging tools, particularly a dual-modal imaging agent that seamlessly incorporates the advantages of both PET and optical imaging, could definitively improve the outcomes in patients with PDAC.

Monoclonal antibodies (mAbs) can provide the necessary specificity, sensitivity, and flexibility for the development of such tools. PET imaging with a radiolabeled mAb (immunoPET) would enhance our ability to noninvasively detect small lesions and slowly growing epithelial cancers (12–14). Near-infrared fluorescent (NIRF) dyes are particularly attractive in intraoperative applications because they show good tissue penetration (up to 1 cm) and low background from autofluorescence. Optical imaging with a NIRF-labeled mAb would allow surgeons to precisely identify tumor margins during resection, ensuring minimal healthy tissue is removed and that no

Significance

Pancreatic cancer will soon be the second leading cause of cancer deaths annually, yet no adequate molecular imaging tools exist to aid in the staging, monitoring, and treatment of the disease. Here we describe the development and preclinical evaluation of three unique immunoconjugates for positron emission tomography, near-infrared fluorescent optical imaging, and multimodal imaging of pancreatic ductal adenocarcinoma (PDAC). The probes were developed using a site-specific, chemoenzymatic methodology that is robust, reproducible, and modular. By targeting CA19.9, the most abundant antigen in >90% of PDAC tumors, we were able to obtain high-quality images in multiple murine models of PDAC, suggesting these constructs could be the core of a molecular imaging toolkit aimed at improving outcomes for patients with PDAC.

Author contributions: J.L.H., B.M.Z., and J.S.L. designed research; J.L.H., B.M.Z., and D.A.-A. performed research; R.A., R.S., B.J.A., and W.W.S. contributed new reagents/analytic tools; J.L.H., B.M.Z., D.A.-A., R.A., R.S., B.J.A., W.W.S., and J.S.L. analyzed data; and J.L.H., B.M.Z., D.A.-A., R.A., R.S., B.J.A., W.W.S., and J.S.L. wrote the paper.

Conflict of interest statement: W.W.S. is an employee of MabVax and has an equity interest.

This article is a PNAS Direct Submission.

Freely available online through the PNAS open access option.

[1]To whom correspondence should be addressed. Email: lewisj2@mskcc.org.

This article contains supporting information online at www.pnas.org/lookup/suppl/doi:10.1073/pnas.1506542112/-/DCSupplemental.

residual tumor tissue is overlooked. Technological advancements in the clinic are now at a stage that allows clinical translation into humans, providing renewed impetus for the preclinical development of tools for NIRF imaging (15, 16).

CA19.9 (also known as sialyl Lewis[a]) is a ligand for epithelial leukocyte adhesion molecules, and its overexpression is a key event in invasion and metastasis of many cancers, including PDAC (17). CA19.9 is an attractive target for imaging of PDAC because it is the most highly expressed tumor antigen (18, 19) and is minimally expressed in healthy pancreas tissue (20). In fact, the diagnosis of PDAC is often aided by the detection of elevated levels of circulating CA19.9 (21, 22). The promise of CA19.9 as a biomarker of PDAC led to the initiation of several antibody discovery programs (14, 20, 23) and the development of the fully human mAb 5B1, which binds an extracellular epitope of CA19.9 with low nanomolar affinity (23). Recently, we demonstrated that CA19.9 could serve as a target for immunoPET imaging of PDAC, even in the context of circulating antigen (24). Based on those results, we set out to improve and expand upon the usefulness of 5B1 in the context of PDAC imaging.

The canonical methodology for the development of mAbs for PET and/or optical imaging suffers from several shortcomings that are a consequence of the indiscriminate conjugation of chelators or dyes to nucleophilic amino acids. Those shortcomings include the loss of immunoreactivity due to conjugation at the antigen-binding region, random conjugation that leads to poorly defined constructs, and an intrinsic lack of reproducibility, as well as laborious, costly optimization of each novel construct. The combination of glycan engineering and bioorthogonal "click" chemistry has proved a successful strategy for conjugating molecules distal to the antigen-binding region of mAbs in a manner that is highly specific and reproducible, circumventing the aforementioned problems (25, 26). Specifically, using a site-specific conjugation strategy for affixing chelator and/or dye molecules via the heavy chain glycans leads to well-defined, robust immunoconjugates in a highly reproducible manner that requires minimal optimization and results in a minimal loss of immunoreactivity. Furthermore, conjugation via the heavy chain glycans offers an exceptional opportunity to construct site-specific, dual-modal immunoconjugates, which are otherwise challenging to develop using traditional conjugation methodology.

Herein, we describe the development of three distinct immunoconjugates that were site-specifically conjugated with DFO for radiolabeling with ^{89}Zr and PET imaging, a NIRF dye for optical imaging, or a dual-labeled construct with both DFO and NIRF dye combining the advantages of PET and NIRF into a single construct. Using the site-specific, bioorthogonal conjugation strategy produced well-defined constructs that retained high levels of immunoreactivity compared with their nonspecifically labeled counterparts. The dual-labeled 5B1 construct, in particular, showed excellent uptake in murine models of PDAC, including delineation of small metastases and dissemination of antigen to sentinel lymph nodes in an orthotopic model.

Results and Discussion

Site-Specific Modification of 5B1. A recently developed chemoenzymatic strategy for the site-specific modification of antibodies was used in the creation of all of the 5B1 immunoconjugates (Fig. 1*A*). This methodology harnesses enzymatic transformations and the strain-promoted azide–alkyne cycloaddition reaction (Fig. S1) to specifically modify the biantennary *N*-linked oligosaccharide chains on the heavy chain of the antibody. By specifically targeting the heavy chain glycans for bioconjugation, this methodology prevents the inadvertent conjugation of payloads to the antigen-binding domains of the antibody—and the consequent reduction in immunoreactivity—that can occur when using non-site-specific, amine-reactive bifunctional molecules. This site-specific modification approach is composed of three steps: (*i*) the removal of the terminal galactose residues of the heavy chain glycans using β-1,4-galactosidase; (*ii*) the attachment of an azide-bearing galactose sugar

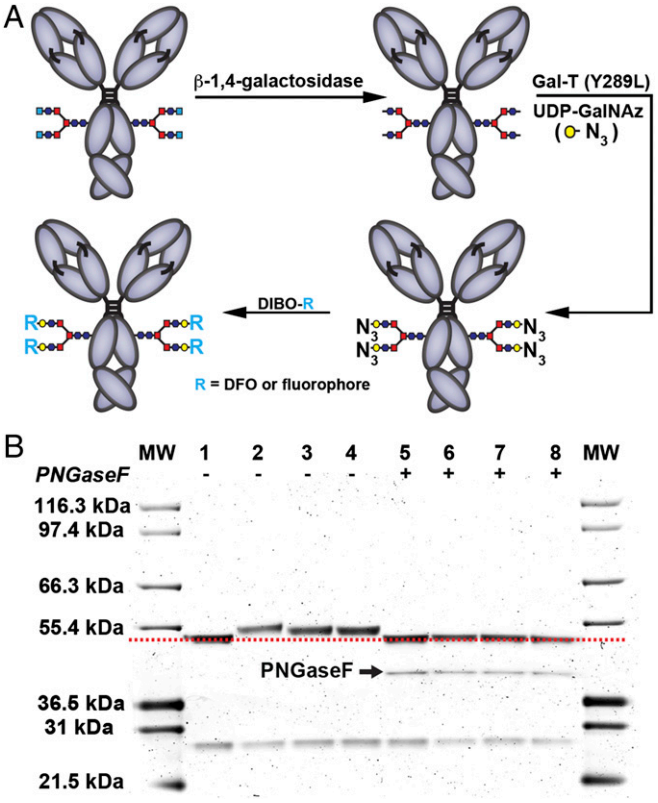

Fig. 1. Strategies for assembling the 5B1 immunoconjugates and their subsequent characterization. (*A*) The enzyme-mediated, site-specific modification of the heavy chain glycans followed by the click chemistry-mediated installation of fluorophores and/or chelators. (*B*) The biochemical analysis of the three reported constructs was carried out via SDS/PAGE gel. Unmodified 5B1 (lanes 1 and 5), ^{ss}DFO-5B1 (lanes 2 and 6), ^{ss}dual-5B1 (lanes 3 and 7), and ^{ss}FL-5B1 (lanes 4 and 8) are shown after treatment with PNGaseF (lanes 1–4) or without treatment (lanes 5–8). The residual PNGaseF (lanes 4–8, 36.5 kDa) is indicated with a black arrow and molecular weight standards are in the first and last lanes (MW).

(GalNAz) to the heavy chain glycans, using a promiscuous galactosyltransferase, GalT(Y289L); and (*iii*) the strain-promoted click conjugation of payload-bearing dibenzocyclooctyne (DIBO) moieties to the azide-bearing galactose residues. In some cases, when a chelator has been appended to the antibody to create a radiolabeling precursor, an additional step is required: (*iv*) the radiometalation of the immunoconjugate.

For the investigation at hand, ^{89}Zr-labeled, fluorophore-labeled, and dual-labeled 5B1 immunoconjugates were synthesized using DIBOs bearing either the $^{89}Zr^{4+}$ chelator desferrioxamine (DIBO-DFO) or a fluorophore with a tissue-penetrating, near-infrared 800-nm emission (DIBO-FL). Over the course of the procedure, the multistep yields for site-specific DFO-5B1 (^{ss}DFO-5B1), ^{ss}FL-5B1, and ^{ss}Dual-5B1 were 75 ± 15%, 78 ± 14%, and 84 ± 16%, respectively ($n = 3$). The degree of labeling (DOL) of the ^{ss}FL-5B1 and ^{ss}Dual-5B1 were 1.5 ± 0.1 and 1.1 ± 0.1 fluorophores per mAb, respectively. Notably, this value is well below the degree of labeling previously obtained using this methodology with other dyes and payloads (~3.5 moieties per mAb) and may be the result of the large and hydrophobic nature of the near-infrared fluorophore. However, these DOL values are ideal as it has been shown that as the ratio of fluorophore to mAb increases toward or beyond 2:1, the uptake of the tracer in nontarget tissues, particularly the liver, increases, leading to decreased tumor uptake and lower tumor to background ratio (27). Additionally, when the ratio of

fluorophore to mAb increases beyond 2:1, there is a risk of self-quenching that can also lower the efficiency of tracer.

The site-specific nature of the bioconjugation was confirmed using SDS/PAGE experiments (Fig. 1*B*). A distinct increase in the molecular weight (M_r) of the heavy chain of the site-specifically modified immunoconjugates can be seen relative to that of the unmodified 5B1 (Fig. 1*B*, lanes 2–5). Importantly, a similar shift is not observed in the M_r of the light chain, showing that the modification occurs only on the heavy chain of the IgG. Further evidence for the glycan-specific nature of the bioconjugation is provided by treatment of the immunoconjugates with PNGaseF, an amidase that specifically cleaves between the asparagine residue of the Fc domain and the innermost sugar of the heavy chain glycans. As expected, SDS/PAGE experiments reveal that PNGaseF treatment has no effect on the molecular weight of the light chains of any of the 5B1 constructs. However, PNGaseF treatment produces marked downward shifts in the molecular weight of the heavy chains of the site-specifically labeled immunoconjugates. Importantly, the heavy chains of all of the immunoconjugates—unmodified 5B1, ^{ss}DFO-5B1, ^{ss}FL-5B1, and ^{ss}Dual-5B—all shift to the same molecular weight (Fig. 1*B*, lanes 6–8). Taken together, these two sets of experiments clearly illustrate that the modification of the 5B1 antibody occurs site specifically on the heavy chain glycans.

Radiolabeling and in Vitro Evaluation of DFO-Modified Constructs. After confirming that the site-specific modification was successful, the next step was to determine whether the modifications offered an improvement over the traditional nonspecific labeling strategy. To do so, the first step was radiolabeling the two DFO-conjugated constructs, ^{ss}DFO-5B1 and ^{ss}dual-5B1, with ^{89}Zr and to then assess those radiolabeled constructs in vitro. To that end, we used well-established methods for radiolabeling biomolecules with ^{89}Zr in a neutralized oxalate solution to generate ^{89}Zr-^{ss}DFO-5B1 and ^{89}Zr-^{ss}dual-5B1 (13, 28, 29).

For a direct comparison with the previously reported, nonspecifically modified ^{89}Zr-DFO-5B1, we considered the specific activity, averaged over multiple radiolabeling experiments, of the purified bioconjugates as the primary benchmark. The average specific activity of ^{89}Zr-^{ss}DFO-5B1 ($n = 5$) was 5.1 ± 1.1 mCi/mg and for ^{89}Zr-^{ss}dual-5B1 ($n = 5$) it was 1.9 ± 0.7 mCi/mg. In every radiolabeling experiment, the radiochemical purity of the purified constructs was >98%. Although both of the site-specifically labeled constructs had a lower specific activity than the nonspecifically labeled construct, which touted a rather impressive 12.1 ± 1.14 mCi/mg, the specific activities were in a suitable range for in vivo experiments. In fact, previous studies with 5B1 had shown that lowering the effective specific activity of 5B1 was beneficial, and in fact necessary, in the context of murine models that shed CA19.9 from the site of the primary tumor into the bloodstream. In such cases, it is important to inject enough of the radiotracer to ensure that a sufficient amount can reach and bind its target at the tumor even if some is sequestered in the blood. Taking this into consideration, the lower specific activity of the site-specifically modified 5B1 constructs is expected to circumvent the need to add "cold" antibody in the context of shed antigen.

A second and perhaps more important benchmark for comparing the site-specific and nonspecific conjugation strategies is the effect on the constructs' antigen binding. The site-specific strategy ensures that modification of 5B1 occurs distal to the antigen-binding site whereas nonspecific conjugation runs the risk of appending a chelator or fluorophore proximal to the antigen-binding site, thereby disrupting the ability of 5B1 to bind CA19.9. So, it makes sense to expect that the immunoreactivity would be improved using the site-specific methodology. To assess the immunoreactivity of ^{89}Zr-^{ss}DFO-5B1 and ^{89}Zr-^{ss}dual-5B1, a well-established in vitro assay (30) was performed using both BxPC3 and MIAPaCa-2 cells, which are CA19.9 positive and CA19.9 negative, respectively. Our analysis showed that the immunoreactivity of the ^{89}Zr-^{ss}DFO-5B1 to BxPC3 was in excess of 98% whereas the immunoreactivity of ^{89}Zr-^{ss}dual-5B1 was in excess of 90%. These results confirmed that the site-specific labeling strategy yielded constructs with improved immunoreactivity relative to the nonspecifically modified ^{89}Zr-DFO-5B1, which had an immunoreactivity of 72.4 ± 1.1% (24). By improving the immunoreactivity by more than 20%, we expect that the site-specifically modified constructs will offer enhanced in vivo behavior compared with nonspecifically modified ^{89}Zr-DFO-5B1. We complemented these studies with a cell-based 96-well plate binding study of the ^{89}Zr-^{ss}dual-5B1 and ^{ss}FL-5B1 constructs, which showed that both had low nanomolar affinity for CA19.9 (Fig. S2). Ultimately, the site-specific bioconjugation strategy produced reliable and robust immunoconjugates that retain their binding properties and are structurally well defined.

Acute Biodistribution of ^{ss}Dual-5B1. To directly quantify the uptake of the radiolabeled ^{89}Zr-^{ss}dual-5B1, the acute biodistribution of the radiotracers was determined at 48 h and 120 h in athymic, nude mice ($n = 4$) bearing a single BxPC3 s.c. xenograft on the right flank (Fig. 2*A* and Table S1). Although the bilateral model showed negligible uptake in the imaging experiments described later, it was not used for the acute biodistribution study. Instead, we chose to use a single xenograft model to allow for a direct comparison with the previous experiments using ^{89}Zr-DFO-5B1 that was not site-specifically modified.

The acute biodistribution data indicated that the uptake of ^{89}Zr-^{ss}dual-5B1 in the BxPC3 xenografts at 48 h [83.5 ± 9.4% injected dose (ID)/g] and 120 h (102.9 ± 26.0% ID/g) was exceptional. However, comparison with the previously reported acute biodistribution data with ^{89}Zr-DFO-5B1 (Table S1) shows that the overall uptake in the tumors is approximately the same at both time points, begging the question of whether the improvement in immunoreactivity resulting from the site-specific labeling

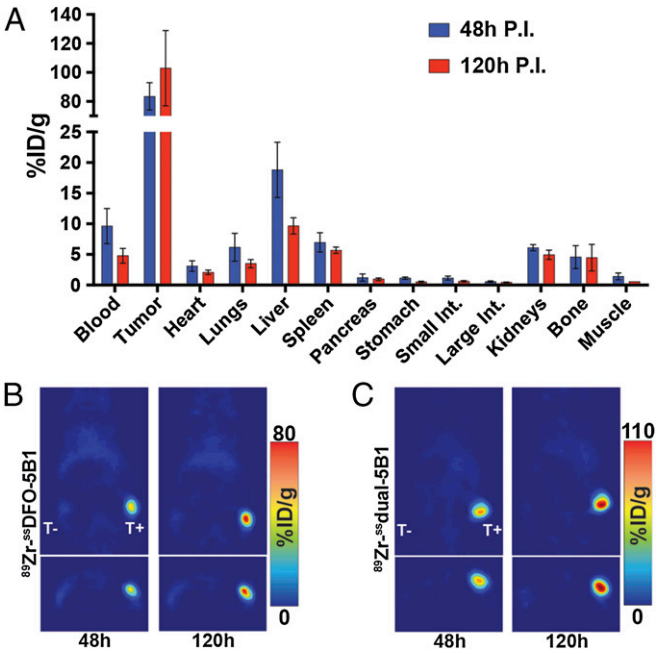

Fig. 2. In vivo distributions of the radiolabeled constructs. (*A*) A graph of the uptake of ^{89}Zr-^{ss}dual-5B1 at 48 h and 120 h in mice bearing a single BxPC3 (CA19.9-positive) tumor determined by acute biodistribution. Error bars represent the SD ($n = 4$). Serial PET imaging of ^{89}Zr-^{ss}DFO-5B1 (*B*) and ^{89}Zr-^{ss}dual-5B1 (*C*) is also shown. Coronal (*B* and *C*, *Top*) and transverse (*B* and *C*, *Bottom*) slices of a representative mouse from each imaging cohort ($n = 3$) are shown. The uptake is reported in percentage of the injected dose per gram of tissue (% ID/g).

of the ^{89}Zr-^{ss}dual-5B1 is reflected in the biodistribution data. When considering PET or NIRF imaging of PDAC in a clinical setting, it will be most important to achieve contrast between the tumor and four organs in particular: the pancreas, the spleen, the kidneys, and the liver. This is simply due to the pancreas residing in direct contact with the liver and spleen in the human body.

Of the nontarget tissues, the accumulation of ^{89}Zr-^{ss}dual-5B1 was highest in the liver at 48 h (18.8 ± 4.5% ID/g), but that value was significantly reduced at 120 h (9.7 ± 1.3% ID/g) to give a tumor to liver ratio of greater than 10:1. In fact, a comparison of ^{ss}dual-5B1 to ^{89}Zr-DFO-5B1 reveals that ^{89}Zr-^{ss}dual-5B1 displayed lower retention in every nontarget tissue at 120 h with the exception of the liver, which was a modest 3% ID/g higher with ^{89}Zr-^{ss}dual-5B1. Considering the drastic improvement in immunoreactivity, the increased uptake in the liver relative to ^{89}Zr-DFO-5B1 is likely the result of appending a fluorescent dye to the antibody, which is known to increase liver uptake in dual-labeled constructs (27).

A better reflection of the effects of site-specific modification is the retention of ^{ss}dual-5B1 in the spleen at 120 h. Rapid uptake and retention of molecules in the spleen are commonly associated with large particles (i.e., nanoparticles and liposomes), and in the case of mAb radiotracers, such uptake is often the result of aggregation. Compared with ^{89}Zr-DFO-5B1, the retention in the spleen was greatly reduced (7.0% ID/g vs. 19.8% ID/g) with ^{ss}dual-5B1. The immunoreactivity of ^{89}Zr-^{ss}dual-5B1 was ∼20% higher, and comparison of the previously reported data suggests this was likely—at least to some extent—due to aggregation of the nonspecifically modified ^{89}Zr-DFO-5B1. The question becomes whether this nearly threefold decrease in spleen retention is offset by the increased uptake of ^{89}Zr-^{ss}dual-5B1 in the liver. Due to the close proximity of the human pancreas to the liver and spleen, it is important that the uptake in any neoplastic tissue is high enough to make it apparent in a PET scan, especially in the context of metastases in those tissues. So, the overall increase in contrast between the tumor and the liver/spleen is perhaps the best benchmark. Overall, the increased contrast of ^{89}Zr-^{ss}dual-5B1 compared with ^{89}Zr-DFO-5B1 is entirely apparent in the spleen whereas the decrease in liver contrast is negligible, suggesting ^{89}Zr-^{ss}dual-5B1 will likely offer advantages in a clinical setting.

In Vivo Imaging with ^{ss}DFO-5B1, ^{ss}FL-5B1, and ^{ss}Dual-5B1. After confirming the ability of each construct to bind CA19.9 in vitro, the next step was to assess each of the three constructs, using in vivo murine models of pancreatic cancer. It has been established that convincingly blocking the binding of radiolabeled 5B1 to CA19.9 using an excess of cold 5B1 is very difficult due to the exceptionally high copy number of CA19.9 in BxPC3 xenografts. In a previous study, a statistically significant level of blocking was achieved by coinjecting an excess of unmodified 5B1, yet the uptake of the 5B1 radiotracer at 24 h postinjection (p.i.) remained in excess of 50% ID/g (24). For that reason, we chose to use a bilateral, s.c. xenograft model, using both a CA19.9-positive (BxPC3) and a CA19.9-negative (MIAPaCa-2) xenograft in each mouse for our PET and NIRF imaging studies to more clearly show the specificity of the site-specifically modified constructs. This allowed each mouse to serve as its own control and reduced the number of mice required. To that end, athymic, nude mice (n = 3 per construct) bearing both a MIAPaCa-2 and BxPC3 s.c. xenografts on either the left or the right flank, respectively, were used to evaluate ^{89}Zr-^{ss}DFO-5B1, ^{ss}FL-5B1, and ^{89}Zr-^{ss}dual-5B1 in vivo.

Both the ^{ss}DFO-5B1 and ^{ss}dual-5B1 exhibited exceptional uptake in BxPC3 tumors that increased over time and negligible uptake in MIAPaCa-2 tumors (Fig. 2 *B* and *C* and Figs. S3 and S4). Regions of interest (ROI) drawn on the PET images (n = 3 per construct) suggested that the uptake in the BxPC3 xenografts was more than eightfold higher than in the MIAPaCa-2 xenografts at 120 h for both constructs (Fig. S5). Large molecules like antibodies are known to accumulate in xenografts, due to the enhanced permeability and retention (EPR) effect, which is likely the reason for the nominal uptake of the radiotracers in the MIAPaCa-2 tumors.

Although visualizing two-dimensional tumor slices allows for a quantitative "snapshot" of the tracers' distribution, considering the maximum intensity projections (MIPs) provides a more complete picture of the PET imaging results. In the case of ^{89}Zr-^{ss}DFO-5B1 and ^{89}Zr-^{ss}dual-5B1, the MIPs indicated that the tumor to background contrast was exceptional in all cases for each of the mice (Figs. S3 and S4). With both constructs, analysis of the MIPs showed some uptake in nontarget tissue that varied between mice, but the nonspecific uptake was quite low and was not consistently high in any one tissue other than the CA19.9-positive xenografts. The higher specific activity of the ^{89}Zr-^{ss}DFO-5B1 construct reduced the time required to obtain quality images, but the overall quality of the images that were acquired with ^{89}Zr ^{ss}dual-5B1 was equal and the uptake values from ROI analysis of the images were slightly higher, reinforcing the results of the acute biodistribution study (Fig. S5).

Concurrent with the PET imaging studies, NIRF imaging was performed with ^{ss}FL-5B1 (Fig. 3*A* and Fig. S6) and ^{89}Zr-^{ss}dual-5B1 (Fig. 3*B* and Fig. S7), the latter using the same cohort of mice from the PET studies discussed above. ^{ss}FL-5B1 (50 μg) was injected into athymic, nude mice (n = 3) with bilateral tumors as described above. The NIRF signal from the tracers in the CA19.9-positive tumors increased over time whereas signal from the nontarget organs and CA19.9-negative tumors was negligible, yielding images of remarkable quality. Similar to the trend seen in the PET images, ^{89}Zr-^{ss}dual-5B1 matched or exceeded its singly modified counterpart, ^{ss}FL-5B1.

After removal of the tumors, the MIAPaCa-2 tumor and remaining organs were harvested for further imaging and analysis ex vivo. NIRF images of the tumors (Fig. S8*A*) and organs (Fig. S8*B*) were acquired to compare the relative fluorescence signal from the whole organs without obstruction by other organs. The average fluorescence signal from BxPC3 tumors was more than 18-fold higher than that of the MiaPaCa-2 tumors and the tumor to organ ratios were all in excess of 25:1 (Fig. S8*C*). The contrast achieved in both the in vivo and ex vivo NIRF images, particularly with the ^{89}Zr-^{ss}dual-5B1 construct, further confirmed the specificity of the tracers and provided us further impetus to carry the ^{89}Zr-^{ss}dual-5B1 forward to studies in more advanced murine models of PDAC.

In Vivo Imaging ^{89}Zr-^{ss}Dual-5B1 in an Orthotopic Model of PDAC. After establishing the potential of ^{89}Zr-^{ss}dual-5B1 in initial PET and NIRF imaging studies, we assessed it in a mouse model that more accurately recapitulates the tumor environment found in PDAC. We transitioned to an orthotopic pancreatic cancer model in which the lesions are formed directly in the pancreas, using a different human PDAC cell line, Suit-2. Suit-2 tumors are known to shed CA19.9 into the blood, which occurs more often than not in PDAC and is the basis of the CA19.9 blood test that is the current standard for evaluating PDAC patients in a clinical setting (31, 32). Furthermore, Suit-2 tumors that are inoculated in the pancreas are known to metastasize and thus provide a better platform for evaluating the potential for clinical translation of these radiotracers (31).

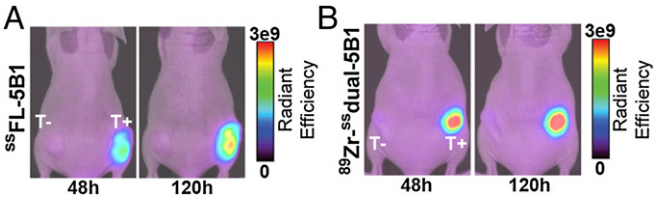

Fig. 3. (*A* and *B*) Serial NIRF imaging using ^{ss}FL-5B1 (50 μg) (*A*) and ^{89}Zr-^{ss}dual-5B1 (50 μg, 92 ± 14 μCi) (*B*). NIRF images of a representative mouse from each cohort (n = 3) bearing CA19.9-negative (T−, left flank) and CA19.9-positive (T+, right flank) tumors that were acquired at 48 h and 120 h are shown. The scale of the fluorescence signal is reported as radiant efficiency [(p/s/cm^2/sr)/(μW/ cm^2)].

Our goal was to study the ^{89}Zr-^{ss}dual-5B1 in a model that provides the best recapitulation of CA19.9-positive PDAC in a clinical setting that is currently possible with a murine model. Each of the orthotopically implanted mice developed primary pancreatic tumors and one mouse, which was selected for further PET-computed tomography (PET/CT) imaging, had additionally developed multiple metastases in the abdominal cavity that could be clearly delineated in the PET images (Fig. 4*A*). PET/CT imaging provided an accurate anatomic localization of the PET signal, suggesting at least two large metastases in the abdominal cavity (Fig. 4*B*). Additionally, the images clearly delineated the sentinel lymph nodes, suggesting potential metastasis or lymphatic drainage from the tumors due to shedding CA19.9. The involvement of the lymphatic system in metastases has been well documented, and the ability to map the sentinel lymph nodes noninvasively—as well as in the context of biopsy or surgical resection—could prove beneficial in a clinical setting. Stage 2 PDAC is characterized by spread to the lymph nodes, and ^{ss}dual-5B1 could reliably guide the biopsy of the appropriate sentinel lymph nodes. Although ^{ss}dual-5B1 cannot directly determine whether malignancy has spread to the sentinel lymph nodes, the information provided by an image-guided biopsy could prove crucial to the staging and, consequently, treatment of PDAC.

After PET/CT imaging at 120 h, the mouse was killed and NIRF images of the intact mouse were acquired. The initial images showed the primary tumor, sentinel lymph nodes, and the primary metastases that had been identified in the PET/CT images. The NIRF signal was used to aid in the localization and removal of several of the sentinel lymph nodes (Fig. 4*C*). An image with an expanded view of the open abdominal cavity after removal of the sentinel lymph nodes shows the remaining lymph nodes as well as the primary tumor (Fig. 4*D*). Interestingly, NIRF signal was also apparent in numerous micrometastases that were not delineated in the PET/CT scans and were in most cases not obvious to the naked eye. After NIRF imaging was completed, a portion of a large liver metastasis and the pancreas, including the primary tumor, were collected for ex vivo analysis. Due to the large number of micrometastases and partial infiltration of the primary tumor into the spleen, it was not possible to remove all of the tumor tissue. Nonetheless, this study did illustrate the remarkable potential of ^{89}Zr-^{ss}dual-5B1 to serve as a guide for the staging, treatment planning, and resection of PDAC. In particular, the delineation of micrometastases that were not apparent to the naked eye or in the PET imaging could prove beneficial. The diagnosis of metastatic disease precludes patients with PDAC from resection. However, it is not uncommon for metastases to go undetected, resulting in futile resection procedures that greatly decrease the quality of life of a patient that has no hope of being cured. The application of ^{89}Zr-^{ss}dual-5B1 in resection candidates could prevent such needless resections by aiding in the detection of difficult to identify metastases.

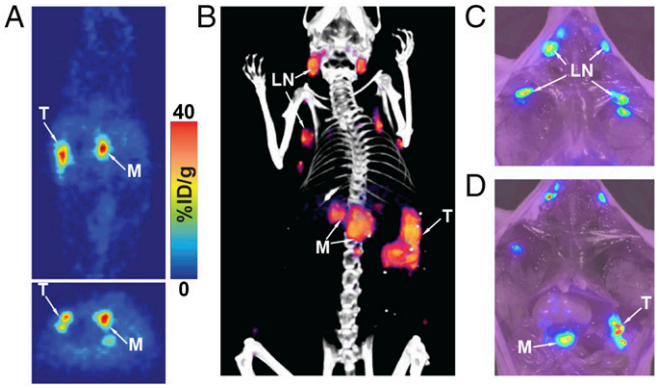

Fig. 4. PET, PET/CT, and NIRF imaging of ^{89}Zr-^{ss}dual-5B1 (50μg, 84 ± 6 μCi) in an orthotopic PDAC model. (*A*) Slices (*Top*, coronal; *Bottom*, transverse) of a representative mouse at 120 h p.i. show high uptake in the primary tumor, a metastasis, and sentinel lymph nodes (LN, lymph node; M, metastasis; T, tumor). (*B*) A rendering of the PET/CT data allows for the anatomization of the lesions. (*C* and *D*) NIRF imaging of the sentinel lymph nodes (*C*) and the open thoracic cavity (*D*) after removal of the LNs demonstrates the potential of ^{89}Zr-^{ss}dual-5B1 in an intraoperative setting.

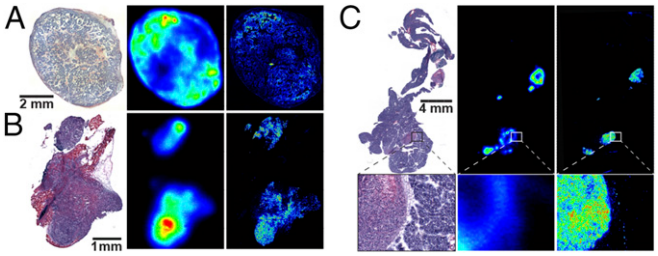

Fig. 5. Histology (*A–C*, *Left*), autoradiography (*A–C*, *Center*), and fluorescence microscopy (*A–C*, *Right*) of resected tumor tissue from mice injected with ^{89}Zr-^{ss}dual-5B1. (*A*) A BxPC3 xenograft, (*B*) metastatic foci from a mouse with a Suit-2 orthotopic xenograft, and (*C*) the primary tumor with surrounding healthy pancreas tissue from the same mouse are shown, confirming colocalization of the tracer with CA19.9 expression.

Ex Vivo Evaluation of ^{ss}DFO-5B1, ^{ss}FL-5B1, and ^{ss}Dual-5B1. To demarcate the areas of specific uptake and demonstrate preferential localization of the ^{89}Zr-^{ss}dual-5B1, tissues of interest were harvested for ex vivo analysis directly after the completion of the imaging studies. A representative BxPC3 tumor from a mouse injected with ^{89}Zr-^{ss}dual-5B1 is shown in Fig. 5*A*. The histologic staining and the autoradiography confirmed that the uptake of ^{89}Zr-^{ss}dual-5B1 was focused in areas of the highest CA19.9 expression. Autoradiography of MIAPaCa-2 tumor slices showed no detectable signal, suggesting the small amount of ^{89}Zr-^{ss}dual-5B1 seen in the PET and NIRF imaging was due to nonspecific accumulation (Fig. S9*A*).

Tumor tissues were also harvested from the mouse with an orthotopic Suit-2 xenograft that underwent PET/CT and postmortem NIRF imaging. A portion of the metastases located in the liver (Fig. 5*B*) was harvested as was the primary pancreatic tumor with the surrounding pancreas tissue (Fig. 5*C*). The distribution of ^{89}Zr-^{ss}dual-5B1 in the small metastasis matched the expression of the CA19.9, and the same was true of the primary tumor in the pancreas, which was easily distinguished from the healthy pancreas (Fig. 5*C*, *Inset*). Examination of the right brachial lymph node, which showed a strong signal by PET, showed that the accumulation was nonspecific (Fig. S9*B*), and histological evaluation confirmed no tumor cells were present.

Conclusions

Currently, there are no clinically available, PDAC-specific molecular imaging tools, and FDG is not well suited for imaging PDAC. We have generated an array of three modular tools to do exactly that by targeting the most common clinical biomarker in PDAC, CA19.9. The three constructs that we evaluated—^{89}Zr-^{ss}DFO-5B1, ^{ss}FL-5B1, and ^{89}Zr-^{ss}dual-5B1—displayed excellent uptake in CA19.9-positive xenograft models of PDAC, suggesting that each of them has the potential to improve outcomes in patients with PDAC. One of these constructs, ^{89}Zr-^{ss}dual-5B1, combines the strengths of PET and optical imaging into a single agent, using a robust, reproducible, and modular methodology that does not compromise the binding to CA19.9. Evaluation of ^{89}Zr-^{ss}dual-5B1 in an orthotopic PDAC model demonstrated that the dual-modal construct has multiple applications, including PET imaging to stage PDAC and identify small metastases, visualization of malignant tissue during tumor resection, and localization of sentinel lymph nodes using PET and/or optical modalities. Although these results represent a

major step toward developing a clinically useful toolkit for the management of PDAC, it is worth noting that mice do not naturally express CA19.9, making it impossible to determine how the background expression of CA19.9 will influence imaging contrast. Inflammation associated with pancreatitis is known to increase CA19.9 expression and could also reduce image contrast. We are collaboratively working to develop a mouse model in which CA19.9 is constitutively expressed to provide a platform to study these effects and further optimize our CA19.9 probes.

Materials and Methods

Construct Preparation and Characterization. The 5B1 was modified to incorporate four azido groups (^{ss}5B1-N_3) by a previously reported method (25, 26) and then was incubated with DIBO-DFO, DIBO-FL, or a 1:1 mixture of the two constructs to create the completed immunoconjugates: ^{ss}DFO-5B1, ^{ss}FL-5B1, and ^{ss}Dual-5B1. An SDS/PAGE assay was performed, as previously described (25, 26), to demonstrate the specificity of the conjugation. For biodistribution and imaging studies, the ^{ss}DFO-5B1 and ^{ss}Dual-5B1 were radiolabeled following published procedures to generate ^{89}Zr-^{ss}DFO-5B1 and ^{89}Zr-^{ss}dual-5B1 (13, 28, 29). Radiolabeled constructs were analyzed by radio-TLC to assess the radiochemical purity and a cell-based binding assay to assess the immunoreactivity, using previously described methods. The DOL for ^{ss}FL-5B1 was determined via UV-Vis spectrophotometry at 280 nm and 774 nm per the dye manufacturer's instruction.

Murine Models. All experiments involving laboratory animals were performed in accordance with the Memorial Sloan Kettering Institutional Animal Care and Use Committee (protocol 08–07-013). BxPC3 and MIAPaCa-2 xenografts were grown 18–21 d postimplantation. Orthotopic pancreas tumors were induced via intrapancreatic injection of Suit-2 cells into the body of the pancreas and were allowed to develop for 14 d before PET, PET/CT, and NIRF imaging.

Acute Biodistribution. The acute biodistribution of ^{89}Zr-^{ss}dual-5B1 was determined in mice with BxPC3 s.c. xenografts. Mice (n = 4) were injected with ^{89}Zr-^{ss}dual-5B1 via the lateral tail vein and euthanized at 48 h and 120 h p.i. before collection of 13 tissues, including the tumor. The mass of each organ was determined and then each sample was counted using an automatic gamma counter. Counts were converted into activity (% ID/g)—after decay and background correction—by normalization to the total activity injected into the respective animal.

In Vivo Imaging. For imaging, mice (n = 3) were injected via the lateral tail vein with an equal mass (50 μg) of the appropriate imaging agent. At 24 h, 48 h, 72 h, and 120 h p.i., PET and/or NIRF images of mice were acquired. Mice with orthotopic Suit-2 xenografts were injected with ^{89}Zr-^{ss}dual-5B1 and images were acquired at 48 h and 120 h on a small animal PET/CT scanner.

Ex Vivo Analysis. Tissues were resected, embedded, and frozen in optimal cutting temperature compound, and sequential 10-μm sections were cut for analysis. Autoradiography was performed in a film cassette on a phosphor imaging plate. Immunohistochemistry (IHC) was performed with unmodified 5B1 that was visualized with a fluorescently labeled goat anti-human secondary antibody. A sequential section was submitted to the Memorial Sloan Kettering Cancer Center (MSKCC) Molecular Cytology Core Facility for automated hematoxylin and eosin staining.

ACKNOWLEDGMENTS. We thank the staff of the MSKCC Small Animal Imaging Core Facility as well as the Radiochemistry and Molecular Imaging Probe core, which were supported in part by NIH Grant P30 CA08748. The authors also thank the NIH [1F32CA180452-01A1 and 5R25CA096945-09 (to J.L.H.), 2R42CA128362 and HHSN261201300060C (to W.W.S.), and 1K99CA178205-01A1 and 4R00CA178205-02 (to B.M.Z.)].

1. Siegel R, Naishadham D, Jemal A (2013) Cancer statistics, 2013. *CA Cancer J Clin* 63(1):11–30.
2. Rahib L, et al. (2014) Projecting cancer incidence and deaths to 2030: The unexpected burden of thyroid, liver, and pancreas cancers in the United States. *Cancer Res* 74(11):2913–2921.
3. Kalser MH, Barkin J, MacIntyre JM (1985) Pancreatic cancer. Assessment of prognosis by clinical presentation. *Cancer* 56(2):397–402.
4. Jemal A, Siegel R, Xu J, Ward E (2010) Cancer statistics, 2010. *CA Cancer J Clin* 60(5):277–300.
5. Cameron JL, Riall TS, Coleman J, Belcher KA (2006) One thousand consecutive pancreaticoduodenectomies. *Ann Surg* 244(1):10–15.
6. van Dam GM, et al. (2011) Intraoperative tumor-specific fluorescence imaging in ovarian cancer by folate receptor-α targeting: First in-human results. *Nat Med* 17(10):1315–1319.
7. Keogan MT, et al. (1998) Diagnosis of pancreatic carcinoma: Role of FDG PET. *AJR Am J Roentgenol* 171(6):1565–1570.
8. Higashi T, et al. (2003) Diagnosis of pancreatic cancer using fluorine-18 fluorodeoxyglucose positron emission tomography (FDG PET) –usefulness and limitations in "clinical reality". *Ann Nucl Med* 17(4):261–279.
9. Frohlich A, et al. (1999) Detection of liver metastases from pancreatic cancer using FDG PET. *J Nuclear Med* 40(2):250–255.
10. Murakami K (2011) FDG-PET for hepatobiliary and pancreatic cancer: Advances and current limitations. *World J Clin Oncol* 2(5):229–236.
11. Koyama K, et al. (2001) Diagnostic usefulness of FDG PET for pancreatic mass lesions. *Ann Nucl Med* 15(3):217–224.
12. Adams GP, et al. (1998) Prolonged in vivo tumour retention of a human diabody targeting the extracellular domain of human HER2/neu. *Br J Cancer* 77(9):1405–1412.
13. Holland JP, et al. (2010) 89Zr-DFO-J591 for immunoPET of prostate-specific membrane antigen expression in vivo. *J Nuclear Med* 51(8):1293–1300.
14. Girgis MD, et al. (2011) Anti-CA19-9 diabody as a PET imaging probe for pancreas cancer. *J Surg Res* 170(2):169–178.
15. Hussain T, Nguyen QT (2014) Molecular imaging for cancer diagnosis and surgery. *Adv Drug Deliv Rev* 66:90–100.
16. Sevick-Muraca EM (2012) Translation of near-infrared fluorescence imaging technologies: Emerging clinical applications. *Annu Rev Med* 63:217–231.
17. Kannagi R, Izawa M, Koike T, Miyazaki K, Kimura N (2004) Carbohydrate-mediated cell adhesion in cancer metastasis and angiogenesis. *Cancer Sci* 95(5):377–384.
18. Loy TS, Sharp SC, Andershock CJ, Craig SB (1993) Distribution of CA 19-9 in adenocarcinomas and transitional cell carcinomas. An immunohistochemical study of 527 cases. *Am J Clin Pathol* 99(6):726–728.
19. Makovitzky J (1986) The distribution and localization of the monoclonal antibody-defined antigen 19-9 (CA19-9) in chronic pancreatitis and pancreatic carcinoma. An immunohistochemical study. *Virchows Arch B Cell Pathol Incl Mol Pathol* 51(6):535–544.
20. Magnani JL, Steplewski Z, Koprowski H, Ginsburg V (1983) Identification of the gastrointestinal and pancreatic cancer-associated antigen detected by monoclonal antibody 19-9 in the sera of patients as a mucin. *Cancer Res* 43(11):5489–5492.
21. Humphris JL, et al. (2012) The prognostic and predictive value of serum CA19.9 in pancreatic cancer. *Ann Oncol* 23(7):1713–1722.
22. Sugiura T, et al. (2012) Serum CA19-9 is a significant predictor among preoperative parameters for early recurrence after resection of pancreatic adenocarcinoma. *J Gastrointest Surg* 16(5):977–985.
23. Sawada R, et al. (2011) Human monoclonal antibodies to sialyl-Lewis (CA19.9) with potent CDC, ADCC, and antitumor activity. *Clin Cancer Res* 17(5):1024–1032.
24. Viola-Villegas NT, et al. (2013) Applying PET to broaden the diagnostic utility of the clinically validated CA19.9 serum biomarker for oncology. *J Nuclear Med* 54(11):1876–1882.
25. Zeglis BM, et al. (2014) Chemoenzymatic strategy for the synthesis of site-specifically labeled immunoconjugates for multimodal PET and optical imaging. *Bioconjug Chem* 25(12):2123–2128.
26. Zeglis BM, et al. (2013) Enzyme-mediated methodology for the site-specific radiolabeling of antibodies based on catalyst-free click chemistry. *Bioconjug Chem* 24(6):1057–1067.
27. Cohen R, Vugts DJ, Stigter-van Walsum M, Visser GW, van Dongen GA (2013) Inert coupling of IRDye800CW and zirconium-89 to monoclonal antibodies for single- or dual-mode fluorescence and PET imaging. *Nat Protoc* 8(5):1010–1018.
28. Holland JP, Sheh Y, Lewis JS (2009) Standardized methods for the production of high specific-activity zirconium-89. *Nucl Med Biol* 36(7):729–739.
29. Verel I, et al. (2003) 89Zr immuno-PET: Comprehensive procedures for the production of 89Zr-labeled monoclonal antibodies. *J Nuclear Med* 44(8):1271–1281.
30. Lindmo T, Bunn PA, Jr (1986) Determination of the true immunoreactive fraction of monoclonal antibodies after radiolabeling. *Methods Enzymol* 121:678–691.
31. Iwamura T, et al. (1992) Correlation between CA19-9 production in vitro and histological grades of differentiation in vivo in clones isolated from a human pancreatic cancer cell line (SUIT-2). *J Gastroenterol Hepatol* 7(5):512–519.
32. Iwamura T, Katsuki T (1987) Kinetics of carcinoembryonic antigen and carbohydrate antigen 19-9 production in a human pancreatic cancer cell line (SUIT-2). *Gastroenterol Jpn* 22(5):640–646.